Newton

Article

Tracing the ultrafast buildup and decay of d-d transitions in $FePS_3$

Graphical abstract

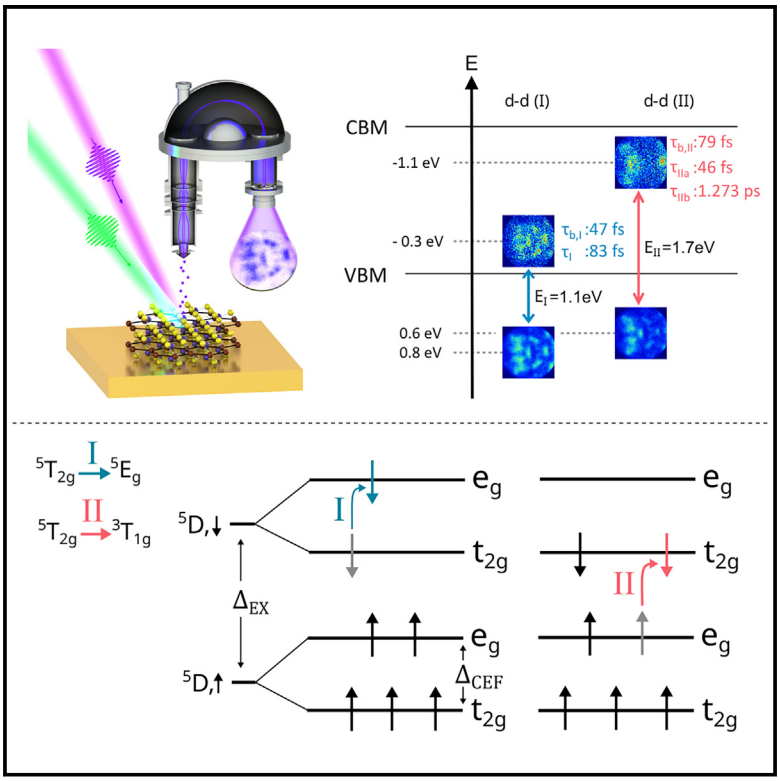

Highlights

- Ultrafast dynamics of spin-allowed and spin-forbidden d-d transitions in $FePS_3$
- Time-resolved ARPES tracks momentum-dependent signatures of d-d transitions
- Exchange and spin-orbit coupling govern distinct relaxation pathways
- Findings offer insights into orbital excitations in quantum materials

Authors

Jonah Elias Nitschke, Lasse Sternemann, Michael Gutnikov, ..., José J. Baldoví, Frithjof Anders, Mirko Cinchetti

Correspondence

jonah.nitschke@tu-dortmund.de (J.E.N.), mirko.cinchetti@tu-dortmund.de (M.C.)

In brief

Time-resolved ARPES reveals the ultrafast dynamics of orbital d-d transitions in $FePS_3$, a van der Waals antiferromagnet. Nitschke et al. demonstrate that the spin-allowed transition exhibits a single decay channel, while the spin-forbidden transition relaxes through two distinct pathways: exchange-mediated virtual hopping and spin-orbit coupling. This study provides a new method to probe and understand below-band-gap orbital transitions in semiconducting and insulating quantum materials with temporal and momentum resolution.

Nitschke et al., 2025, Newton *1*, 100019
April 7, 2025 © 2025 The Author(s). Published by Elsevier Inc.
https://doi.org/10.1016/j.newton.2025.100019

CellPress

Newton

CellPress
OPEN ACCESS

Article

Tracing the ultrafast buildup and decay of d-d transitions in $FePS_3$

Jonah Elias Nitschke,[1,*] Lasse Sternemann,[1] Michael Gutnikov,[1] Karl Schiller,[1] Eugenio Coronado,[2] Alan Omar,[3] Giovanni Zamborlini,[1,5] Clara Saraceno,[3] Matija Stupar,[1] Alberto M. Ruiz,[2] Dorye L. Esteras,[2] José J. Baldoví,[2] Frithjof Anders,[1] and Mirko Cinchetti[1,4,*]

[1]TU Dortmund University, Otto-Hahn-Straße 4, 44227 Dortmund, Germany
[2]Instituto de Ciencia Molecular, Universitat de València, 46980 Paterna, Spain
[3]Photonics and Ultrafast Laser Science, Ruhr-Universität Bochum, Universitätsstrasse 150, 44801 Bochum, Germany
[4]Lead contact
[5]Present address: Institute of Physics, NAWI Graz, University of Graz, Universitätsplatz 5, 8010 Graz, Austria
*Correspondence: jonah.nitschke@tu-dortmund.de (J.E.N.), mirko.cinchetti@tu-dortmund.de (M.C.)
https://doi.org/10.1016/j.newton.2025.100019

ACCESSIBLE OVERVIEW Orbital excitations between localized 3d states, known as d-d transitions, are fundamental to materials science but remain difficult to resolve in time. Using time- and angle-resolved photoelectron spectroscopy (trARPES), this study reports these transitions in $FePS_3$, a van der Waals antiferromagnet. The study reveals distinct ultrafast dynamics for spin-allowed and spin-forbidden transitions, shedding light on their relaxation mechanisms. This work extends the capabilities of trARPES, enabling the study of orbital transitions in correlated materials with temporal and momentum resolution.

SUMMARY

Excitations between localized 3d states of transition metal ions within crystalline solids, commonly known as d-d transitions, play a pivotal role in diverse phenomena across solid-state physics, materials science, and chemistry. Until now, an experimental method to unravel the complex quasiparticle dynamics associated with d-d transitions has remained elusive. In this study, we bridge this gap by demonstrating that d-d transitions can be distinctly traced both in momentum space and in time using time- and angle-resolved photoelectron spectroscopy (trARPES). As a model system, we select $FePS_3$, a two-dimensional van der Waals antiferromagnet with a rich array of quantum phenomena stemming from d-d transitions. Our investigation reveals the ultrafast dynamics of both a spin-allowed ($^5T_{2g} \rightarrow {}^5E_g$) and a spin-forbidden ($^5T_{2g} \rightarrow {}^3T_{1g}$) d-d transition within the Fe^{2+} multiplet. We observe that for off-resonant excitation, the spin-allowed excitation exhibits a quicker buildup compared to the spin-forbidden transition, and it decays with a single exponential behavior over a timescale of 83 fs. For the spin-forbidden transition, we identify two independent decay channels with decay constants of 46 and 1,273 fs that we attribute to an exchange-mediated virtual hopping between neighboring Fe^{2+} ions and an on-site spin-orbit-mediated spin-flip process, respectively.

INTRODUCTION

Excitations between 3d states of transition metal (TM) ions in crystalline solids play a crucial role in determining the optical and electronic properties of materials. These optical transitions are typically forbidden under the electric-dipole approximation due to the Laporte rule.[1] However, various effects, such as the mixing of orbitals with opposite parity due to vibronic coupling[2,3] or inversion symmetry breaking at magnetic ions,[4] can lead to weak absorption. Although this absorption is usually only about 10^{-3} times the intensity of symmetry-allowed transitions, d-d transitions often influence the color of TM oxides[5] and are pivotal in catalytic processes on oxide surfaces.[6] In Cu-O-based perovskites, the interaction between localized Cu 3d holes and more delocalized O 2p holes, leading to the formation of a Zhang-Rice singlet,[7] is fundamental for high-temperature superconductivity.[1]

In the realm of van der Waals (vdW) magnets, particularly TM phosphorus trisulfides ($TMPS_3$s), the TM electrons are predominantly localized at the TM sites. This localization suggests a similar phenomenology related to d-d transitions to that observed in TM oxides. Importantly, when the TM equals Fe, Co, Ni, or Mn, these compounds exhibit behavior characteristic of two-dimensional (2D) antiferromagnets. The magnetic moments are primarily localized on the TM ions (Mn^{2+}, Fe^{2+}, Co^{2+}, and Ni^{2+}) and arise from the interplay between crystal field

This is an open access article under the CC BY license (http://creativecommons.org/licenses/by/4.0/).

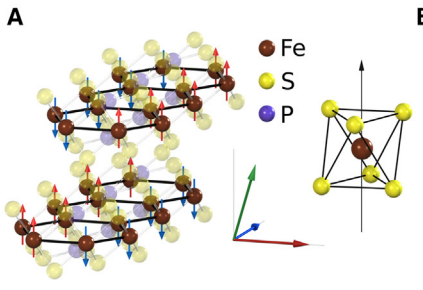

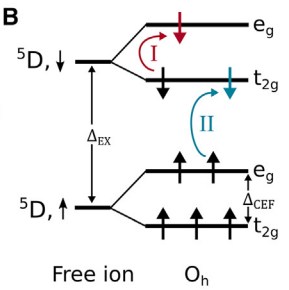

C

Transition	Energy (eV)
$^5T_{2g} \rightarrow {}^5E_g$	1.08
$^5T_{2g} \rightarrow {}^3T_{1g}$	1.78
$^5T_{2g} \rightarrow {}^3T_{2g}$	2.14
$^5T_{2g} \rightarrow {}^3T_{1g}$	2.46
$^5T_{2g} \rightarrow {}^3T_{2g}$	2.58
$^5T_{2g} \rightarrow {}^3T_{1g}$	2.84

Figure 1. $FePS_3$ crystal structure and d-d transitions

(A) Crystal structure of $FePS_3$ showing the iron atoms (brown) in a hexagonal structure surrounded by sulfur (yellow) and phosphor (blue) bipyramidals. The octahedral coordination of sulfur atoms around iron results in crystal field splitting.

(B) d orbitals splitting into t_{2g} and e_g orbitals. The arrows symbolize the spin associated with the corresponding electron in the different orbitals. The spin-conserving $^5T_{2g}$ (t_{2g}^4 e_g^2) → ^5E_g (t_{2g}^3 e_g^3) transition, denoted with I, has an energy of 1.1 eV. The first spin-forbidden $^5T_{2g}$ (t_{2g}^4 e_g^2) → $^3T_{1g}$ (t_{2g}^4 e_g^2) transition (II) is observed at an excitation energy of 1.8 eV.

(C) Energy of the first six d-d transitions in $FePS_3$ according to Joy et al.[20]

splitting and exchange splitting. It is plausible to anticipate that an excitation of the (d^5, d^6, d^7, d^8) multiplets would be coupled to magnetic excitations as well as lattice distortions, as the d-d transitions are known to induce static and dynamic Jahn-Teller effects.[8]

Recent studies have indeed unveiled that in the XY-type antiferromagnet $NiPS_3$, d-d transitions can generate electron-phonon bound states[9] and selectively activate magnon modes with sub-THz frequency.[10] Coherent excitonic excitations based on Zhang-Rice states, consisting of a hole spin in a localized Ni 3d orbital and a hole spin delocalized over the 3p orbitals of the adjacent ligands, have also been documented in $NiPS_3$.[11] These spin-orbit entangled excitons were demonstrated to be intrinsically coupled to the antiferromagnetic (AF) order[11,12] and, later, used to generate a novel transient conducting AF state.[13] More recent studies based on ultra-high energy resolution resonant inelastic X-ray scattering (RIXS) have led to the description of such excitations as Hund's excitons.[14] In the Ising-type antiferromagnet $FePS_3$, the excitation of a d-d transition of the Fe^{2+} multiplet has been shown to generate coherent THz optical lattice and hybridized phonon-magnon modes,[15] a phenomenon aligning with the strong coupling between AF magnons and optical phonons reported in 2D AF materials.[16–18]

Despite their pivotal role, the dynamics and lifetimes of d-d transitions remain largely unexplored. Understanding these aspects is crucial for harnessing d-d transitions to manipulate the functional properties of 2D quantum materials. Early investigations employing optical absorption spectroscopy[19,20] and X-ray photoelectron spectroscopy[21] elucidated the spectral features arising below the band gap in various $TMPS_3$ crystals ($NiPS_3$, $FePS_3$, $ZnPS_3$, and $MnPS_3$) and attributed them to transitions within the d-electron manifold of the corresponding TM atom in octahedral symmetry. These findings facilitated the determination of the crystal field D_q and the Racah interelectron repulsion parameter B, establishing these materials as ionic compounds with localized d states.

In this work, we delve into $FePS_3$, aiming to introduce multidimensional time- and angle-resolved photoelectron spectroscopy (trARPES)[22–26] as a potent experimental technique to bridge the existing knowledge gap concerning the transient dynamics of d-d transitions. $FePS_3$ is a vdW AF semiconductor with a band gap of approximately 1.4 eV,[27–31] and its electronic properties can be elucidated, to a first approximation, using an ionic model.[21] This model features covalently bonded $(PS_3)_2^{2-}$ clusters, with the sulfur atoms leading to an octahedral crystal field (O_h) around the Fe^{2+} ions (see Figure 1A), whose localized 3d levels are affected by strong electronic correlations. Given that the top of the valence band and the bottom of the conduction band are formed mainly by the Fe 3d states,[27,31,32] $FePS_3$ can be classified as a Mott-Hubbard-type insulator.[27] Consequently, its low-energy electronic configuration is primarily governed by the Fe 3d states.[29]

In $FePS_3$, the octahedral crystal field generated by the sulfur atoms leads to a splitting of the different Fe^{2+} d orbitals into two energy levels—the t_{2g} (containing d_{xy}, d_{xz}, and d_{yz}) and e_g (containing d_{z2} and d_{x2-y2}) orbitals. Here, the ground state $^5T_{2g}$ (t_{2g}^4 e_g^2) and the lowest excited electronic state ^5E_g (t_{2g}^3 e_g^3) emerge from the ground term (^5D) of d^6. The transition between these two states ($^5T_{2g}$ → ^5E_g), hereafter referred to as transition I between the t_{2g} and e_g orbitals, is the only spin-allowed transition within the crystal-field-split Fe^{2+} multiplet. The leading single-particle contribution of this d-d transition is depicted in Figure 1B. In contrast, the other possible transitions within this multiplet, with the lowest energy transition ($^5T_{2g}$ → $^3T_{1g}$) labeled as transition II in Figure 1B, are spin forbidden and have been rarely studied because of their weak nature. In general, depending on their energy (Figure 1C), d-d transitions either appear in the optical absorption spectra (see Figure S1) as a very weak and broad feature centered around approximately 1.1 eV (transition I) or are masked by the enhanced absorption occurring with the onset of the band gap at around 1.5 eV[20] (higher energy transitions).

RESULTS

Experimental scheme and rationale of the experiments

To showcase the capability of trARPES in capturing the ultrafast dynamics of intra-ionic d-d transitions in $FePS_3$, we conducted pump-probe experiments utilizing two specifically chosen pump

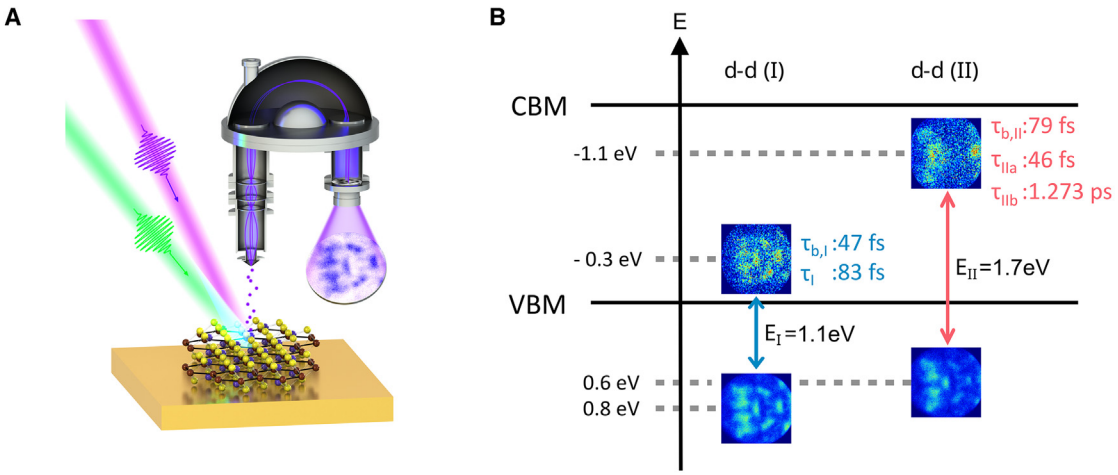

Figure 2. Experimental configuration and relevant energy- and timescales

(A) Schematic representation of the pump-probe setup used to investigate the electron dynamics in $FePS_3$. First, the pump pulse (green) impinges on the sample and excites dynamics that are subsequently probed by the XUV probe pulse (violet) and analyzed with a momentum microscope.

(B) Schematic representation of the relevant energies and time constants in our trARPES experiments. The small insets represent the momentum maps (I vs. k_x,k_y) at the different characteristic energies marked by the dashed gray lines. The ARPES features related to d-d transitions stem from excitations containing multiple single-particle contributions and, as such, cannot be simply described with a band structure picture.

photon energies: $h\nu_1$ = 1.2 eV and $h\nu_2$ = 2.4 eV. These energies were selected to fall below and above the band gap of $FePS_3$, respectively. Employing these photon energies, we optically excite $FePS_3$ and analyze the resulting d-d transition dynamics using p-polarized extreme ultraviolet (XUV) probe pulses with a photon energy of 21.7 eV and a momentum microscope, as illustrated in Figure 2A (see methods for more details). To avoid pump- or probe-induced space charge as well as charging effects due to the bad electrical conductivity of $TMPS_3$ materials, the shape of the photoemission spectrum was monitored in dependence of both the pump and the XUV pulse fluence, to choose a regime where no static changes in the shape of the valence band spectrum are observable (more details in supplemental methods). The experiments were performed at room temperature (T = 300 K), which corresponds to the paramagnetic phase of $FePS_3$, as cooling below the Neél temperature leads to strong charging effects, prohibiting photoemission experiments.

For the identification of the distinctive signature of d-d transitions in trARPES, we are examining states above the valence band maximum (VBM)—a region where ARPES intensity is observable solely after optical excitation (see Figure 2B). To achieve this, we generate transient ARPES maps by calculating the difference between the measured ARPES intensity at specific time delays and an average from a 200 fs window prior to t_0 = 0 fs, marking the temporal overlap of pump and probe beams. This methodology enables the clear identification of excited states (non-equilibrium spectra) and their comparison to static ARPES measurements, indicative of the ground state in the absence of pump beam excitation (equilibrium spectra). In the case of the d-d transitions observed here, we emphasize that these are not single-particle excitations; rather, they involve multiple electrons within the $3d^6$ multiplet of the $Fe2^+$ ion in $FePS_3$. Consequently, the observed spectral features cannot be interpreted solely within a band structure framework, as they represent a collective excitation. This scenario is analogous to excitons in trARPES, where the photoemission signature reflects the electron-hole nature of the compound quasiparticle rather than individual electronic states.[33,34]

As depicted in Figure 2B, by pumping the system with 1.2 eV, we resonantly excite the spin-conserving transition I, enabling the determination of its decay constant (τ_I). Pumping with a photon energy of 2.4 eV places us off-resonance with d-d transitions but above the band gap, causing electron excitation from the valence to the conduction band. We then monitor how electrons in the conduction band decay to the conduction band minimum (CBM), including the buildup times of transitions I and II ($\tau_{b,I}$ and $\tau_{b,II}$, respectively), as well as the decay mechanisms of transition II. In the following, we will demonstrate that this spin-forbidden transition decays through two independent channels, labeled as τ_{IIa} and τ_{IIb}.

Below-band-gap excitation

We start by reporting the experiments performed with an excitation energy of $h\nu_1$ = 1.2 eV, which is below the band gap and in resonance with the spin-allowed $^5T_{2g} \rightarrow {}^5E_g$ transition I. Figure 3A shows the differential angle-integrated signal from the non-equilibrium ARPES spectra, acquired with a pump fluence of 380 μJ/cm^2. For consistency, the energy of photoelectrons is always referenced to the VBM, determined from static measurements. The bottom of the color scale corresponds to no changes in comparison to the equilibrium, while the maximum represents strong additional intensity. The data uncover a signal, extending up to −0.9 eV, that decays on a timescale of a few-hundred femtoseconds and retains consistent time-dependent characteristics across all energy levels. To increase the statistics for extraction of the decay constant, we integrate the signal in a 300 meV broad window between −0.3 and −0.6 eV, which is shown in Figure 3B together with a fit consisting of a Gaussian convoluted with a

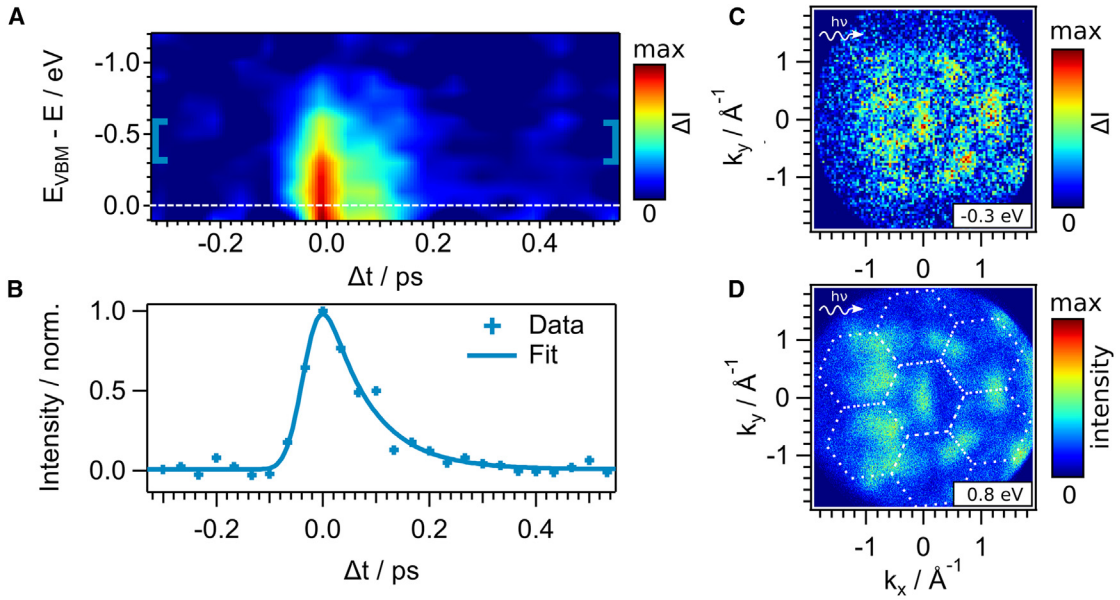

Figure 3. Visualization and analysis of dynamics for $h\nu_1$ = 1.2 eV excitation

(A) Differential angle-integrated non-equilibrium transient signal following optical excitation with 1.2 eV pump photons, interpolated with a bilinear algorithm. The color gradient spans from blue (no difference) to dark red (positive difference). The blue bracket highlights the energy region used for subsequent analysis.

(B) Normalized photoemission intensity derived by integrating between −0.3 and −0.6 eV.

(C) Non-equilibrium momentum map measured at −0.3 eV at temporal overlap, giving information about the excited state.

(D) Equilibrium momentum map measured at 0.8 eV, giving information about the ground state. The dotted white hexagons represent the first Brillouin zone (BZ) as well as the neighboring BZ.

single exponential decay. The decay constant and the corresponding error bar extracted from the fit is τ_I = 83 ± 10 fs.

Based on the observed transient signal, we want to investigate now in more detail the momentum-resolved ARPES intensity captured at temporal overlap (details on data analysis are provided in Figures S3 and S4). An exemplarily non-equilibrium momentum map recorded 300 meV above the VBM (excited states) at temporal overlap is visualized in Figure 3C and compared to the equilibrium momentum map recorded 800 meV below the VBM (occupied states) and visualized in Figure 3D. In these momentum maps, due to the high angular acceptance of our momentum microscope (±90°) and the large unit cell of $FePS_3$, we can observe the signal stemming from the first as well as the neighboring Brillouin zones (BZs) without tilting the sample. For reference, the BZs are indicated by the white dashed hexagons in Figure 3D. To interpret the observed constant energy contours, it is essential to consider the stacking configuration in multilayer $FePS_3$, where layers are shifted along the a axis of the crystal. This shift introduces an additional symmetry component that affects the overall symmetry of the iso-energy contours. Our density functional theory (DFT) calculations (DFT+U) in Nitschke et al.[31] show that, at certain energies, hexagonal symmetry is not fully preserved, even in theoretically generated iso-energy maps (see supplemental methods). This observation is consistent with recent findings from similar materials.[29,35] Furthermore, in our prior work,[31] we demonstrated that the valence band near the VBM predominantly comprises Fe d orbitals, confirming the orbital contribution that characterizes the features observed in our data.

The momentum maps reveal a complex fingerprint, with higher intensities at the Γ-point of the 1st BZ and the M-points of the first and neighboring BZs. The most striking observation is the strong similarity of the non-equilibrium map in Figure 3C—related to the excited state—to the equilibrium momentum map in Figure 3D, which corresponds to the ground state. As mentioned above, previous static ARPES data[31] have shown that the spectral weight of the static momentum map stems mainly from the Fe d orbitals, raising the question of why the intensity distribution in the non-equilibrium momentum map is almost identical. Given the energy difference of 1.1 eV between the two momentum maps, corresponding to the energy of transition I, we attribute the non-equilibrium momentum map to the unique ARPES fingerprint of the $^5T_{2g} \rightarrow {}^5E_g$ transition, with its electronic components being captured by the XUV probe pulse. It is important to note that the asymmetric nature of the observed transient signal around t_0, along with its presence under s-polarized pump light, allows us to rule out laser-assisted photoemission[36] as the origin of the non-equilibrium momentum map (details in Figure S5). Further insights are provided in the discussion section below.

Above-band-gap excitation

When we examine excitation with a pump energy of $h\nu_2$ = 2.4 eV, the results differ significantly from the earlier discussed pump energy of $h\nu_1$ = 1.2 eV. Specifically, an excitation above the band gap using $h\nu_2$ = 2.4 eV with a pump fluence of 470 μJ/cm^2 presents a more intricate scenario. Figure 4A presents the angle-integrated signal from the non-equilibrium ARPES spectra for energies up

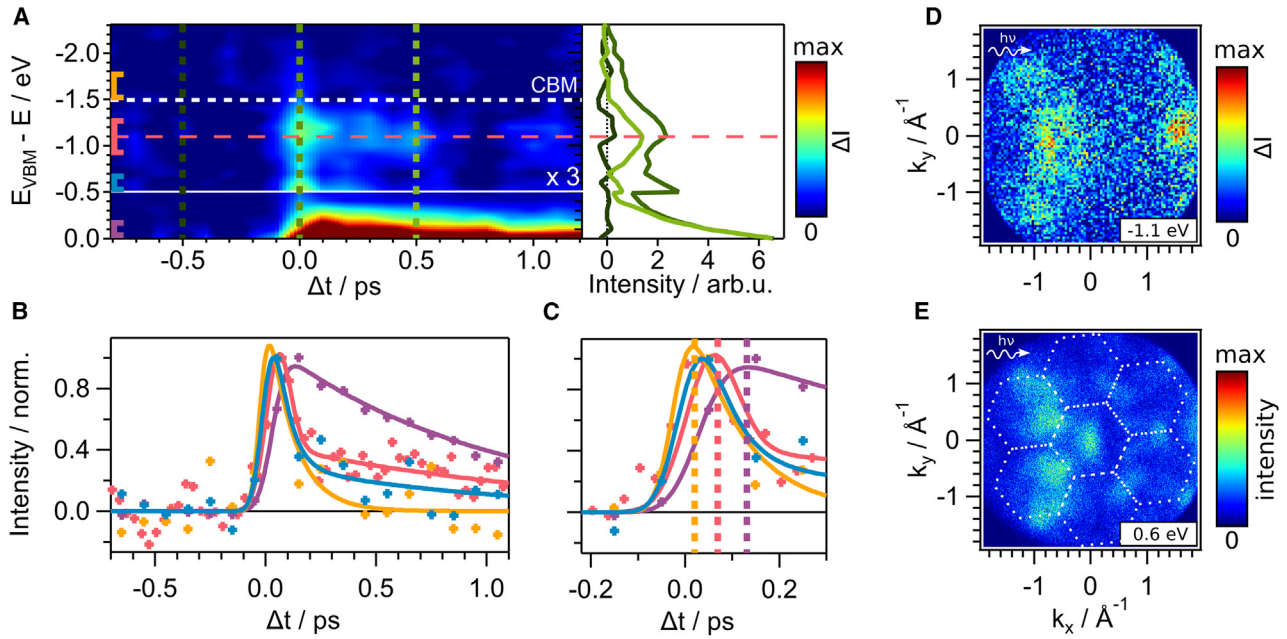

Figure 4. Visualization and analysis of dynamics for $h\nu_2$ = 2.4 eV excitation

(A) Angle-integrated non-equilibrium transient signal following optical excitation with 2.4 eV pump photons, processed through bilinear interpolation for smoother visualization. Signals above −0.5 eV have been amplified by a factor 3 for enhanced clarity. The right side shows the energy distribution curve (EDC) profiles at 3 different time steps (marked by dotted lines in corresponding shades of green), revealing a long-lived Gaussian feature centered around −1.1 eV (marked by the red dotted line). Differently colored brackets on the left axis represent specific energy ranges integrated to generate the normalized traces shown in (B).

(C) Close-up of the data in (B) around the transient signal peaks.

(D) Non-equilibrium momentum map at −1.1 eV, captured 50 fs after temporal overlap.

(E) Equilibrium momentum map recorded at 0.6 eV. The dotted white hexagons represent the first Brillouin zone (BZ) as well as the neighboring BZ.

to −2.4 eV. In contrast to the observations from the sub-band-gap excitation, unique behaviors emerge across different energy regions. Color-coded brackets (yellow, red, blue, and purple) mark these energy regions, with the corresponding normalized photoemission intensity transients shown in Figure 4B. The transient signal in the yellow region around −1.75 eV manifests a single exponential decay with a time constant of τ_{CBM} = 115 ± 100 fs. This rapid decay is evident across all energies above the CBM, which is located around −1.4 eV.[28] Venturing slightly below the CBM, we observe a roughly 600 meV broad window centered around −1.1 eV (red brackets) that exhibits a double exponential decay. For a closer investigation of these two components, we performed additional measurements with a 3 times smaller step size of 33 fs (red curve in Figure 4B). This unveils a fast decay constant of $\tau_{II,a}$ = 46 ± 34 fs and a long-lived contribution with $\tau_{II,b}$ = 1,273 ± 268 fs.

To understand the states involved in the dynamics discussed above, we proceed as in the previous section and disclose the momentum map at −1.1 eV. Figure 4D shows the non-equilibrium momentum map captured at this energy 50 fs after temporal overlap of both pulses, at the peak of the red transient. This map displays a distinct k-dependent pattern, with peak intensities bordering the first BZ. When comparing this pattern with the equilibrium momentum map recorded at 0.6 eV (Figure 4E), we again identify a resemblance between non-equilibrium and equilibrium momentum maps. In this case, however, the energetic difference between the two maps is around 1.7 eV, and the resemblance is not as identical as observed in experiments with below-band-gap excitation. In the next section, we will use this information to provide a complete picture of the observed transient dynamics and assign the transient momentum maps to the spin-forbidden transition II in Figure 1B.

We now continue describing the transient signal in Figure 4A. The purple brackets mark a 200 meV energy window around the VBM, where the signal shows a single exponential decay, with a decay constant of τ_{purple} = 973 ± 66 fs. The photoemission signal in this energy region is contributed to weak pump-induced thermal broadening[37] due to the high absorption in the case of above-band-gap excitation, which appears quite strong in comparison to the induced changes above the VBM in Figure 4A, as the graph only depicts the absolute difference (more details in Figure S6). This is also in agreement with the below-band-gap excitation, where no such changes in the valence band after excitation are observed, as the absorption is strongly reduced for hν = 1.2 eV.

As photoluminescence measurements suggest that above-band-gap excitation should also excite lower-energy d-d transitions,[38] we examine the subtle transient signal between −0.5 and −0.7 eV (blue brackets) where, according to the previous section, we expect the signal from the $^5T_{2g} \rightarrow {}^5E_g$ transition. The transient trace shown with a blue curve in Figure 4B indeed contains two decay components, where the slower-decaying component

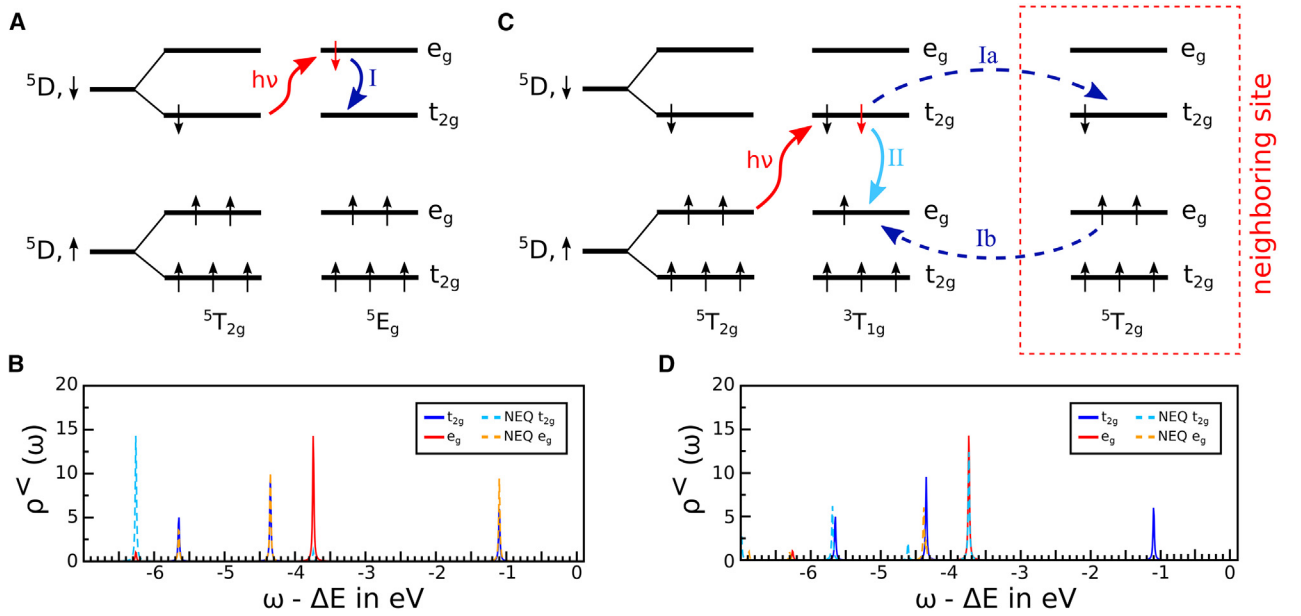

Figure 5. Schematic representation of the multiplet state of the ground state and excited states and the corresponding calculations of the lesser Green function

(A) Changes in the Fe^{2+} ion multiplet state after exciting the energetically lowest-lying d-d transition with $h\nu_1$ = 1.2 eV. The arrows symbolize the spin associated with the corresponding electron in the different orbitals. This is the only transition possible without involving a spin flip due to a spin-conserving transition from the spin-down t_{2g} orbital into the e_g orbital (shown by the red arrow).

(B) The equilibrium spectra of the lesser Green function for the t_{2g} (blue) and e_g (red) orbitals, as well as the non-equilibrium (NEQ) calculations depicted in dashed lines with the corresponding colors, shifted by the excitation energy of ΔE = 1.0786 eV.

(C and D) The second-lowest d-d transition involves a spin flip with an electron from the spin-up t_{2g} orbital now occupying the spin-down t_{2g} orbital (C). This excitation can either propagate via virtual hopping to a neighboring side (IIa) or relax via SOC including a spin-flip transition (IIb). The corresponding equilibrium and NEQ spectra (shifted by the excitation energy of ΔE = 1.74 eV) are shown in (D) and reveal a slight shift when comparing the different orbital peaks with a complete absence of the lowest excitation peak for the NEQ spectrum.

can be ascribed to the signal from the VBM dynamics, while the faster component has a decay constant $\tau_{I,2.4\ eV}$ = 66 ± 128 fs, comparable to the one observed from the $^5T_{2g} \rightarrow {}^5E_g$ transition with $h\nu_1$ = 1.2 eV, i.e., $\tau_{I,1.2\ eV}$ (more details in Figure S7). We thus conclude that excitation with a pump energy of $h\nu_2$ = 2.4 eV generates both transitions I and II, and we can detect both of them in the ARPES spectra.

An additional comparison of the peak position of the different extracted transients in Figure 4C shows a clear delay between the different signals, as indicated by the dotted lines marking the maximum intensity. This suggests that transitions I and II build up on different timescales after optical excitation. In the supplemental methods, we determine the buildup times for transitions I and II by fitting the rising edge with a Gaussian convoluted with an exponential function and calculating the time difference between 10% and 90% of the maximum signal. We obtain $\tau_{b,I}$ = (47 ± 15) fs and $\tau_{b,II}$ = (79 ± 18) fs. Within our experimental time resolution, we can thus conclude that the d-d transition I builds up almost instantaneously and more quickly than transition II.

Localized model for the d-d excitations

To interpret the experimental findings, we start again from our assignment of the observed differential momentum map arising after excitation with 1.2 eV photons to the spin-allowed $^5T_{2g} \rightarrow {}^5E_g$ transition. This assignment can be rationalized by resorting to a simplified description for strongly correlated materials[39] based on the exact diagonalization of all local 3d charge configurations (see methods). In this framework, the Coulomb repulsion U and the Hund's rule exchange J are entered as Racah parameters.[39] The 1.2 eV pump pulse is theorized to induce a spin-allowed d-d transition, essentially transferring an electron from a doubly occupied t_{2g} orbital to a singly occupied e_g orbital, as schematically depicted in Figure 5A. The known excitation energy ΔE = 1.0786 eV determines the crystal electric field splitting Δ_{CEF} of these orbitals.[20] This allows us to calculate the local Fe occupational (or lesser) spectral functions relevant for ARPES (details in supplemental methods). In static ARPES experiments, electrons are photoemitted from the Fe ground-state configuration ($^5T_{2g}$). Conversely, trARPES experiments, particularly following a 1.2 eV pump pulse, involve photoemission from the excited ^5E_g spin multiplet, resulting in a $3d^5$ configuration. This distinction is mirrored in the equilibrium and non-equilibrium atomic spectra, as depicted in Figure 5B. Crucially, the non-equilibrium spectra (shifted by the excitation energy ΔE) and the equilibrium spectra exhibit several identical peaks, with slight differences in spectral weights. Since the atomic Green's functions become the starting point for the lattice spectral functions[40]

and the hybridization between the orbitals remains unaltered by the laser pulse in leading order, the striking similarities between the non-equilibrium momentum maps depicted in Figure 3C and the equilibrium maps in Figure 3D can be well understood within this local Fe 3d picture.

This approach also allows us to interpret the data obtained by above-band-gap excitation. As mentioned before, the non-equilibrium momentum maps measured at −1.1 eV display a pronounced similarity to the momentum maps of the occupied states at 0.6 eV. Given that this feature is too low in energy to be related to a population of the CBM, we ascribe the transient state observed at −1.1 eV to the spin-forbidden $^5T_{2g} \rightarrow {}^3T_{1g}$ transition of the Fe^{2+} multiplet, characterized by an energy difference of 1.7 eV—the energy separation between the momentum maps of the occupied and unoccupied states. Figure 5D presents a comparative analysis between the corresponding equilibrium and non-equilibrium atomic spectra, adjusted by the excitation energy of ΔE = 1.79 eV. In this case, the spectra exhibit common features, though the differences are more pronounced compared to the previous case. This observation is consistent with the fact that the momentum maps in Figures 4D and 4E do not completely mirror each other.

Upon exciting $FePS_3$ with 2.4 eV photons, our analysis reveals an initial population of the conduction band, which then depopulates with a time constant of τ_{CBM} = 115 ± 100 fs. The depopulation of the conduction band is followed by the almost instantaneous excitation of the $^5T_{2g} \rightarrow {}^5E_g$ transition ($\tau_{b,I}$ = (47 ± 15) fs) and a delayed excitation of the spin-forbidden $^5T_{2g} \rightarrow {}^3T_{1g}$ transition within $\tau_{b,II}$ = (79 ± 18) fs. The spin-forbidden $^5T_{2g} \rightarrow {}^3T_{1g}$ transition undergoes a double exponential decay, indicating the presence of two independent decay channels in the relaxation back to the ground state. These two pathways have decay constants of τ_{IIa} = 46 ± 34 fs (instantaneous within our time resolution) and τ_{IIb} = 1,273 ± 268 fs. We associate them, respectively, to a virtual hopping between neighboring sides (exchange mechanism) and a spin-orbit coupling (SOC)-mediated spin-flip process. Figure 5C visually portrays the excitation associated with the $^5T_{2g} \rightarrow {}^3T_{1g}$ transition and its relaxation back to the ground state.

To rationalize the timescale related to the SOC-mediated spin-flip process discussed above, we carried out first-principles calculations that incorporate relativistic effects (detailed in the methods section). Starting from the electronic band structure of $FePS_3$ (Figure S10; Nitschke et al.[31]), we determined the SOC constant for Fe^{2+} to be $\lambda_{SOC} = -113.24$ cm^{-1} (14.04 meV), primarily originating from the Fe^{2+} d orbitals. The negative value of λ_{SOC} reflects the more than half-filled occupied shell of Fe^{2+} (with further details in Table S1). By converting λ_{SOC} in time ($\tau_{SOC} = h/E \cong 300$ fs), we find a reasonable correspondence with the experimentally determined spin-flip timescale $\tau_{red,2}$ = 1,273 ± 268 fs. Additionally, we observe that in $NiPS_3$, the value of $\lambda_{SOC} = -280$ cm^{-1} (34.7 meV) was deemed to be sufficient to mix the ^1E_g and $^3T_{2g}$ excited states,[20] thereby enabling the spin-forbidden $^3A_{2g} \rightarrow {}^1E_g$ transition. Considering that in $NiPS_3$, the energy separation between the SOC-mixed states is 7,900 cm^{-1} (0.98 eV), it is plausible that a similar SOC-mediated mixing of the ^5E_g and $^3T_{1g}$ excited states could also be a viable source for spin relaxation in $FePS_3$. This supposition is bolstered by the fact that the energy difference in $FePS_3$ (0.72 meV) is smaller than that in $NiPS_3$.[20]

DISCUSSION

In summary, we have successfully identified two different d-d transitions in the paramagnetic phase of the vdW semiconductor $FePS_3$. By resonantly and non-resonantly exciting the ^5E_g and $^3T_{1g}$ states, we were able to extract their lifetimes and identify the associated relaxation processes. Furthermore, we were able to assign specific momentum-dependent characteristics to both intra-ionic multiplet excitations in agreement with a theoretical model that adeptly encapsulates the primary microscopic features. We thus conclude that trARPES, when performed with a momentum microscope, can indeed capture the momentum-space signature of d-d transitions. This work extends the formidable suite of trARPES applications, complementing its established proficiency in identifying quasiparticles, such as excitons in molecular compounds[41,42] and light-induced quantum phenomena in 2D materials,[43–45] with the ability to probe the dynamics of orbital transitions. In this regard, a systematic study of the changes introduced by cooling the sample under the Neél temperature would be of high interest, as this should enable one to observe changes in the relaxation rates associated with the magnetic phase as well as the interactions with the phonons described by Mertens at al.[15] and Rao et al.,[46] which only show a non-negligible amplitude below the critical temperature.

METHODS

Sample preparation for photoemission spectroscopy

The samples were produced via chemical vapor transport (CVT) and commercially bought from HQ Graphene. The crystals were glued with a conductive silver epoxy on copper sample holders and exfoliated with commercial scotch tape *in situ* at a base pressure in the low 10^{-8} mbar regime. The surface cleanliness under comparable exfoliation conditions was checked by means of X-ray photoelectron spectroscopy (XPS) for possible contamination with oxygen or carbon. Even under exfoliation in a low 10^{-7} mbar regime, no considerable amount of surface contamination was found (see Figure S12).

Femtosecond momentum microscopy

The experimental setup consists of two major parts, namely, a photoemission electron microscope for ARPES experiments (KREIOS, Specs GmbH), as detailed and benchmarked in Ponzoni et al.,[47] and a home-built system for the generation of fs-XUV radiation.[48] In the following, we briefly describe the experimental setup.

To track the dynamics of the localized d-d excitations between crystal-field-split 3d states of the Fe^{2+} multiplet in $FePS_3$, we used a pump-probe scheme. First, d-d transitions were excited (either directly or indirectly) with light pulses of photon energies 1.2 and 2.4 eV (pump beam). Subsequently, the femto- to picosecond evolution of the excited Fe^{2+} multiplet dynamics was probed with an XUV light pulse (21.6 eV, p-polarized), which photoemits the electron contribution of the multiplet excitation into

the detector (probe beam). The pump and probe beams impinge on the sample at an angle of 68° to the surface normal. The cross-correlation of the pump and probe pulses (i.e., the temporal resolution of the setup) was 49 ± 18.9 fs.

The generation of coherent XUV radiation was driven by a commercial fiber-laser (Carbide, Light Conversion) with a central wavelength of 1,035 nm, a temporal resolution of 242 fs, and an average power of 50 W. The variable repetition rate was set to 600 kHz for the reported measurements, giving a pulse energy of 83 mJ. First, the pulses were compressed to sub-50 fs[49] by spectral broadening with self-phase modulation in a X^3 nonlinear medium, followed by dispersion compensation with two mirrors with -200 fs^2 GDD. Second, the compressed pulses were frequency doubled in a BBO crystal and tightly focused into an Ar gas jet inside a vacuum chamber. Here, high-harmonic generation (HHG) was used to create XUV pulses that were filtered by a pair of grazing-incidence plates followed by an Al filter. Last, the ninth harmonic at 21.7 eV was selected in a monochromator with multilayer mirrors and focused onto the $FePS_3$ crystal. As pump pulse, we collect the fundamental frequency after the BBO crystal and couple it to a motor-controlled delay stage to finely adjust the time difference between pump and XUV probe.

The strength of the KREIOS analyzer is the simultaneous measurement of the in-plane momenta of the photoelectrons within the full photoemission horizon. In the instrument, an immersion lens column generates an image of the lateral distribution of the photoelectrons in the sample plane (x,y), and an additional Fourier lens transforms it into an image of the photoelectron emission angles. The latter contains the momentum distribution of the photoelectrons $I(k_x,k_y)$ with high angular resolution. The photoelectrons are then filtered by the hemispherical-analyzer section of the instrument, which acquires momentum-resolved 2D maps at a fixed and selectable kinetic energy (E, k_x,k_y). For this reason, the instrument is also often called a momentum microscope.[50]

Computational methods

We described the Fe(II) 3d shell by a five-orbital model. The full Hamiltonian comprises single-particle orbital terms and the spin-rotational invariant general Coulomb interaction, parameterized by the Hubbard energy U and Hund's rule exchange interaction J.

The single-orbital energies include crystal electric field splitting between the t_{2g} and e_g orbitals determined by spectroscopic excitation energy $^5T_{2g} \rightarrow {}^5E_g$, $\Delta E = 1.076$ eV[20] and are adjusted such that the ground state contains six electrons. The local Mott excitation $U_{eff} = U\text{-}3J = 2.2$ eV was taken from a recent LDA+U approach to $FePS_3$.[39] The demand to reproduce the lowest experimentally observed $^5T_{2g} \rightarrow {}^3T_{1g}$ transition at $\Delta E = 1.796$ eV determined the two Racah parameters to U = 4.15 eV and J = 0.65 eV. We used the total spin and the total charge as conserved quantum numbers to set up the block diagonal many-body Hamiltonian and determined its spectrum and eigenstates by exact diagonalization of each block. From the results, we calculated the spectrum of the lesser Green's functions describing the removal of an electron from a t_{2g} or e_g orbital of the 3d shell using either the projector onto the ground-state manifold (equilibrium) or the projector onto one of the excited states (non-equilibrium) as the density operator.

The electronic structure, including SOC, was calculated by means of DFT+U+SOC using the projector augmented wave (PAW) method as implemented in the Vienna Ab initio Simulation Package (VASP).[51] We considered vdW interactions between layers using the DFT-D3 method,[52] and the plane-wave cutoff was set to 350 eV. The structural optimizations of atomic coordinates were performed setting force and energy convergence criteria of 0.001 eV/Å and 1.0×10^{-6} eV, respectively. The BZ was sampled with a Γ-centered 4 × 4 × 4 k-point Monkhorst-Pack mesh.[53] To properly describe the strong correlation in the d orbitals of Fe, we adopted a Hubbard $U_{eff} = 2.2$ eV using the simplified version proposed by Dudarev et al.[54] A 1 × 1 × 2 monoclinic cell to account for the AF interlayer coupling was employed.

RESOURCE AVAILABILITY

Lead contact

Further information and requests for resources and reagents should be directed to and will be fulfilled by the lead contact, Mirko Cinchetti (mirko.cinchetti@tu-dortmund.de).

Materials availability

This study did not generate new unique materials.

Data and code availability

The raw data that support the findings of this study are available in the Zenodo database. Any additional information required to reanalyze the data reported in this paper is available from the lead contact upon request.

ACKNOWLEDGMENTS

We acknowledge help from Evgeny Zhukov in recording the absorption spectra. This work was supported by the Deutsche Forschungsgemeinschaft (DFG) through the TRR 142/3, Project A08 and Project dd2D (CI 157/11-1). We acknowledge support from the European Union's Horizon 2020 Research and Innovation Programme under Project SINFONIA, grant 964396, and ERC-StG-101042680 2D-SMARTiES. Financial support from MERCUR "Kooperation" project "Toward an UA Ruhr Ultrafast Laser Science Center" is also acknowledged. The momentum microscope was financed by the DFG through the project INST 212/409 and by the "Ministerium für Kultur und Wissenschaft des Landes Nordrhein-Westfalen." J.J.B. acknowledges the Generalitat Valenciana (CIDEXG/2023/1), and A.M.R. thanks the Spanish MIU (grant no. FPU21/04195).

AUTHOR CONTRIBUTIONS

Conceptualization, J.E.N. and M.C.; methodology, J.E.N., L.S., K.S., A.O., G.Z., and M.S.; investigation, J.E.N., M.G., and L.S.; theory, F.A., A.M.R., D.L.E., and J.J.B.; writing—original draft, J.E.N., F.A., and M.C.; writing—review and editing, J.E.N., K.S., G.Z., A.M.R., D.L.E., J.J.B., F.A., and M.C.; funding acquisition, E.C., C.S., and M.C.; resources, F.A. and M.C.; supervision, G.Z. and M.C.

DECLARATION OF INTERESTS

The authors declare no competing interests.

DECLARATION OF GENERATIVE AI AND AI-ASSISTED TECHNOLOGIES IN THE WRITING PROCESS

During the preparation of this work, the authors used ChatGPT to enhance the quality of writing by improving grammar, style, and clarity. After using

this tool/service, the authors reviewed and edited the content as needed and take full responsibility for the content of the publication.

SUPPLEMENTAL INFORMATION

Supplemental information can be found online at https://doi.org/10.1016/j.newton.2025.100019.

Received: August 29, 2024
Revised: November 20, 2024
Accepted: January 28, 2025
Published: February 20, 2025

REFERENCES

1. Fromme, B. (2001). d-d Excitations in Transition-Metal Oxides, A Spin-Polarized Electron Energy-Loss Spectroscopy (SPEELS) Study. Springer Tr. Mod. Phys. https://doi.org/10.1007/3-540-45342-3.
2. Cotton, F.A. (1990). Chemical Applications of Group Theory, 3rd ed. (Wiley).
3. Grasso, V., Neri, F., Silipigni, L., and Piacentini, M. (1991). NIR-VIS reflectivity spectra of some transition metal thiophosphates. Il Nuovo Cimento D *13*, 633–645. https://doi.org/10.1007/bf02451287.
4. Mikhaylovskiy, R.V., Huisman, T.J., Gavrichkov, V.A., Polukeev, S.I., Ovchinnikov, S.G., Afanasiev, D., Pisarev, R.V., Rasing, T., and Kimel, A.V. (2020). Resonant Pumping of d−d Crystal Field Electronic Transitions as a Mechanism of Ultrafast Optical Control of the Exchange Interactions in Iron Oxides. Phys. Rev. Lett. *125*, 157201. https://doi.org/10.1103/physrevlett.125.157201.
5. Maiman, T.H. (1960). Stimulated Optical Radiation in Ruby. Nature *187*, 493–494. https://doi.org/10.1038/187493a0.
6. Freitag, A., Staemmler, V., Cappus, D., Ventrice, C.A., Al Shamery, K., Kuhlenbeck, H., and Freund, H.-J. (1993). Electronic surface state of NiO (100). Chem. Phys. Lett. *210*, 10–14. https://doi.org/10.1016/0009-2614(93)89091-u.
7. Zhang, F.C., and Rice, T.M. (1988). Effective Hamiltonian for the superconducting Cu oxides. Phys. Rev. B *37*, 3759–3761. https://doi.org/10.1103/physrevb.37.3759.
8. Sugano, S., Tanabe, Y., and Kamimura, H. (1970). Multiplets of Transition-Metal Ions in Crystals (Academic Press). ScienceDirect.com by Elsevier.
9. Ergeçen, E., Ilyas, B., Mao, D., Po, H.C., Yilmaz, M.B., Kim, J., Park, J.-G., Senthil, T., and Gedik, N. (2022). Magnetically brightened dark electron-phonon bound states in a van der Waals antiferromagnet. Nat. Commun. *13*, 98. https://doi.org/10.1038/s41467-021-27741-3.
10. Afanasiev, D., Hortensius, J.R., Matthiesen, M., Mañas-Valero, S., Šiškins, M., Lee, M., Lesne, E., van der Zant, H.S.J., Steeneken, P.G., Ivanov, B.A., et al. (2021). Controlling the anisotropy of a van der Waals antiferromagnet with light. Sci. Adv. *7*, eabf3096. https://doi.org/10.1126/sciadv.abf3096.
11. Kang, S., Kim, K., Kim, B.H., Kim, J., Sim, K.I., Lee, J.-U., Lee, S., Park, K., Yun, S., Kim, T., et al. (2020). Coherent many-body exciton in van der Waals antiferromagnet NiPS3. Nature *583*, 785–789. https://doi.org/10.1038/s41586-020-2520-5.
12. Hwangbo, K., Zhang, Q., Jiang, Q., Wang, Y., Fonseca, J., Wang, C., Diederich, G.M., Gamelin, D.R., Xiao, D., Chu, J.-H., et al. (2021). Highly anisotropic excitons and multiple phonon bound states in a van der Waals antiferromagnetic insulator. Nat. Nanotechnol. *16*, 655–660. https://doi.org/10.1038/s41565-021-00873-9.
13. Belvin, C.A., Baldini, E., Ozel, I.O., Mao, D., Po, H.C., Allington, C.J., Son, S., Kim, B.H., Kim, J., Hwang, I., et al. (2021). Exciton-driven antiferromagnetic metal in a correlated van der Waals insulator. Nat. Commun. *12*, 4837. https://doi.org/10.1038/s41467-021-25164-8.
14. He, W., Shen, Y., Wohlfeld, K., Sears, J., Li, J., Pelliciari, J., Walicki, M., Johnston, S., Baldini, E., Bisogni, V., et al. (2024). Magnetically propagating Hund's exciton in van der Waals antiferromagnet NiPS3. Nat. Commun. *15*, 3496. https://doi.org/10.1038/s41467-024-47852-x.
15. Mertens, F., Mönkebüscher, D., Parlak, U., Boix-Constant, C., Mañas-Valero, S., Matzer, M., Adhikari, R., Bonanni, A., Coronado, E., Kalashnikova, A.M., et al. (2023). Ultrafast Coherent THz Lattice Dynamics Coupled to Spins in the van der Waals Antiferromagnet FePS3. Adv. Mater. *35*, e2208355. https://doi.org/10.1002/adma.202208355.
16. Mai, T.T., Garrity, K.F., McCreary, A., Argo, J., Simpson, J.R., Doan-Nguyen, V., Aguilar, R.V., and Walker, A.R.H. (2021). Magnon-phonon hybridization in 2D antiferromagnet MnPSe3. Sci. Adv. *7*, eabj3106. https://doi.org/10.1126/sciadv.abj3106.
17. Vaclavkova, D., Palit, M., Wyzula, J., Ghosh, S., Delhomme, A., Maity, S., Kapuscinski, P., Ghosh, A., Veis, M., Grzeszczyk, M., et al. (2021). Magnon polarons in the van der Waals antiferromagnet FePS3. Phys. Rev. B *104*, 134437. https://doi.org/10.1103/physrevb.104.134437.
18. Liu, S., Granados Del Águila, A., Bhowmick, D., Gan, C.K., Thu Ha Do, T., Prosnikov, M.A., Sedmidubský, D., Sofer, Z., Christianen, P.C.M., Sengupta, P., and Xiong, Q. (2021). Direct Observation of Magnon-Phonon Strong Coupling in Two-Dimensional Antiferromagnet at High Magnetic Fields. Phys. Rev. Lett. *127*, 097401. https://doi.org/10.1103/physrevlett.127.097401.
19. Banda, E.J.K.B. (2000). Optical absorption of NiPS3 in the near-infrared, visible and near-ultraviolet regions. J. Phys. C Solid State Phys. *19*, 7329–7335. https://doi.org/10.1088/0022-3719/19/36/023.
20. Joy, P.A., and Vasudevan, S. (1992). Optical-absorption spectra of the layered transition-metal thiophosphates MPS3 (M=Mn, Fe, and Ni). Phys. Rev. B *46*, 5134–5141. https://doi.org/10.1103/physrevb.46.5134.
21. Piacentini, M., Khumalo, F.S., Leveque, G., Olson, C.G., and LYNCH, D.W. (1982). X-Ray photoemission and optical spectra of NiPS3, FePS3 and ZnPS3. Chemical Physics *72*, 61–71.
22. Adhikary, G., Saha, T., Ribič, P.R., Stupar, M., Ressel, B., Urbančič, J., Ninno, G.D., Thamizhavel, A., and Maiti, K. (2021). Orbital selective dynamics in Fe-pnictides triggered by polarized pump pulse excitations. Eur. Lett. *136*, 17002. https://doi.org/10.1209/0295-5075/ac2dc0.
23. Nandi, D., Skinner, B., Lee, G.H., Huang, K.-F., Shain, K., Chang, C.-Z., Ou, Y., Lee, S.-P., Ward, J., Moodera, J.S., et al. (2018). Signatures of long-range-correlated disorder in the magnetotransport of ultrathin topological insulators. Phys. Rev. B *98*, 214203. https://doi.org/10.1103/physrevb.98.214203.
24. Rettig, L., Cortés, R., Thirupathaiah, S., Gegenwart, P., Jeevan, H.S., Wolf, M., Fink, J., and Bovensiepen, U. (2012). Ultrafast Momentum-Dependent Response of Electrons in Antiferromagnetic EuFe2As2 Driven by Optical Excitation. Phys. Rev. Lett. *108*, 097002. https://doi.org/10.1103/physrevlett.108.097002.
25. Schmitt, F., Kirchmann, P.S., Bovensiepen, U., Moore, R.G., Rettig, L., Krenz, M., Chu, J.-H., Ru, N., Perfetti, L., Lu, D.H., et al. (2008). Transient Electronic Structure and Melting of a Charge Density Wave in TbTe3. Science *321*, 1649–1652. https://doi.org/10.1126/science.1160778.
26. Brorson, S.D., Kazeroonian, A., Moodera, J.S., Face, D.W., Cheng, T.K., Ippen, E.P., Dresselhaus, M.S., and Dresselhaus, G. (1990). Femtosecond room-temperature measurement of the electron-phonon coupling constant γ in metallic superconductors. Phys. Rev. Lett. *64*, 2172–2175. https://doi.org/10.1103/physrevlett.64.2172.
27. Jin, Y., Yan, M., Kremer, T., Voloshina, E., and Dedkov, Y. (2022). Mott–Hubbard insulating state for the layered van der Waals FePX3 (X: S, Se) as revealed by NEXAFS and resonant photoelectron spectroscopy. Sci. Rep. *12*, 735. https://doi.org/10.1038/s41598-021-04557-1.
28. Budniak, A.K., Zelewski, S.J., Birowska, M., Woźniak, T., Bendikov, T., Kauffmann, Y., Amouyal, Y., Kudrawiec, R., and Lifshitz, E. (2022). Spectroscopy and Structural Investigation of Iron Phosphorus Trisulfide—FePS3. Adv. Opt. Mater. *10*, 202102489. https://doi.org/10.1002/adom.202102489.

29. Koitzsch, A., Klaproth, T., Selter, S., Shemerliuk, Y., Aswartham, S., Janson, O., Büchner, B., and Knupfer, M. (2023). Intertwined electronic and magnetic structure of the van-der-Waals antiferromagnet Fe2P2S6. npj Quantum Mater. *8*, 27. https://doi.org/10.1038/s41535-023-00560-z.

30. Dedkov, Y., Guo, Y., and Voloshina, E. (2023). Progress in the studies of electronic and magnetic properties of layered MPX3 materials (M: transition metal, X: chalcogen). Electron. Struct. *5*, 043001. https://doi.org/10.1088/2516-1075/acfa4e.

31. Nitschke, J.E., Esteras, D.L., Gutnikov, M., Schiller, K., Mañas-Valero, S., Coronado, E., Stupar, M., Zamborlini, G., Ponzoni, S., Baldoví, J.J., and Cinchetti, M. (2023). Valence band electronic structure of the van der Waals antiferromagnet FePS3. Mater. Today Electron. *6*, 100061. https://doi.org/10.1016/j.mtelec.2023.100061.

32. Li, K., Yan, M., Jin, Y., Jin, Y., Guo, Y., Voloshina, E., and Dedkov, Y. (2023). Dual Character of the Insulating State in the van der Waals Fe1–x Ni x PS3 Alloyed Compounds. J. Phys. Chem. Lett. *14*, 57–65. https://doi.org/10.1021/acs.jpclett.2c03492.

33. Reutzel, M., Jansen, G.S.M., and Mathias, S. (2024). Probing excitons with time-resolved momentum microscopy. Adv. Phys. X *9*, 2378722. https://doi.org/10.1080/23746149.2024.2378722.

34. Rustagi, A., and Kemper, A.F. (2018). Photoemission signature of excitons. Phys. Rev. B *97*, 235310. https://doi.org/10.1103/physrevb.97.235310.

35. Strasdas, J., Pestka, B., Rybak, M., Budniak, A.K., Leuth, N., Boban, H., Feyer, V., Cojocariu, I., Baranowski, D., Avila, J., et al. (2023). Electronic Band Structure Changes across the Antiferromagnetic Phase Transition of Exfoliated MnPS3 Flakes Probed by μ-ARPES. Nano Lett. *23*, 10342–10349. https://doi.org/10.1021/acs.nanolett.3c02906.

36. Saathoff, G., Miaja-Avila, L., Aeschlimann, M., Murnane, M.M., and Kapteyn, H.C. (2008). Laser-assisted photoemission from surfaces. Phys. Rev. A *77*, 022903. https://doi.org/10.1103/physreva.77.022903.

37. Golež, D., Dufresne, S.K.Y., Kim, M.-J., Boschini, F., Chu, H., Murakami, Y., Levy, G., Mills, A.K., Zhdanovich, S., Isobe, M., et al. (2022). Unveiling the underlying interactions in Ta2NiSe5 from photoinduced lifetime change. Phys. Rev. B *106*, L121106. https://doi.org/10.1103/physrevb.106.l121106.

38. Ramos, M., Marques-Moros, F., Esteras, D.L., Mañas-Valero, S., Henríquez-Guerra, E., Gadea, M., Baldoví, J.J., Canet-Ferrer, J., Coronado, E., and Calvo, M.R. (2022). Photoluminescence Enhancement by Band Alignment Engineering in MoS2/FePS3 van der Waals Heterostructures. ACS Appl. Mater. Interfaces *14*, 33482–33490. https://doi.org/10.1021/acsami.2c05464.

39. Katsnelson, M.I., and Lichtenstein, A.I. (2010). Theory of optically forbidden d–d transitions in strongly correlated crystals. J. Phys. Condens. Matter. *22*, 382201. https://doi.org/10.1088/0953-8984/22/38/382201.

40. Lichtenstein, A.I., and Katsnelson, M.I. (1998). Ab initio calculations of quasiparticle band structure in correlated systems: LDA++ approach. Phys. Rev. B *57*, 6884–6895. https://doi.org/10.1103/physrevb.57.6884.

41. Wallauer, R., Raths, M., Stallberg, K., Münster, L., Brandstetter, D., Yang, X., Güdde, J., Puschnig, P., Soubatch, S., Kumpf, C., et al. (2021). Tracing orbital images on ultrafast time scales. Science *371*, 1056–1059. https://doi.org/10.1126/science.abf3286.

42. Neef, A., Beaulieu, S., Hammer, S., Dong, S., Maklar, J., Pincelli, T., Xian, R.P., Wolf, M., Rettig, L., Pflaum, J., and Ernstorfer, R. (2023). Orbital-resolved observation of singlet fission. Nature *616*, 275–279. https://doi.org/10.1038/s41586-023-05814-1.

43. Schmitt, D., Bange, J.P., Bennecke, W., AlMutairi, A., Meneghini, G., Watanabe, K., Taniguchi, T., Steil, D., Luke, D.R., Weitz, R.T., et al. (2022). Formation of moiré interlayer excitons in space and time. Nature *608*, 499–503. https://doi.org/10.1038/s41586-022-04977-7.

44. Karni, O., Esin, I., and Dani, K.M. (2023). Through the Lens of a Momentum Microscope: Viewing Light-Induced Quantum Phenomena in 2D Materials. Adv. Mater. *35*, e2204120. https://doi.org/10.1002/adma.202204120.

45. Madéo, J., Man, M.K.L., Sahoo, C., Campbell, M., Pareek, V., Wong, E.L., Al-Mahboob, A., Chan, N.S., Karmakar, A., Mariserla, B.M.K., et al. (2020). Directly visualizing the momentum-forbidden dark excitons and their dynamics in atomically thin semiconductors. Science *370*, 1199–1204. https://doi.org/10.1126/science.aba1029.

46. Rao, R., Selhorst, R., Siebenaller, R., Giordano, A.N., Conner, B.S., Rowe, E., and Susner, M.A. (2024). Mode-Selective Spin–Phonon Coupling in van der Waals Antiferromagnets. Adv. Phys. Res *3*, 2300153. https://doi.org/10.1002/apxr.202300153.

47. Ponzoni, S., Paßlack, F., Stupar, M., Janas, D.M., Zamborlini, G., and Cinchetti, M. (2023). Dirac Bands in the Topological Insulator Bi2Se3 Mapped by Time-Resolved Momentum Microscopy. Adv. Phys. Res *2*, 202200016. https://doi.org/10.1002/apxr.202200016.

48. Schiller, K., Stupar, M., Sternemann, L., Omar, A., Saraceno, M., Nitschke, J., Mischke, V., Janas, D., Ponzoni, S., Zamborlini, G., et al. (2025). Time-resolved momentum microscopy with fs-XUV photons at high repetition rates with flexible energy and time resolution. Sci. Rep. *15*, 3611. https://doi.org/10.1038/s41598-025-86660-1.

49. Mansourzadeh, S., Vogel, T., Omar, A., Shalaby, M., Cinchetti, M., and Saraceno, C.J. (2023). Broadband, high power THz source at 540 kHz using organic crystal BNA. APL Photonics *8*, 011301. https://doi.org/10.1063/5.0126367.

50. Krömker, B., Escher, M., Funnemann, D., Hartung, D., Engelhard, H., and Kirschner, J. (2008). Development of a momentum microscope for time resolved band structure imaging. Review of Scientific Instruments *79*, 053702. https://doi.org/10.1063/1.2918133.

51. Kresse, G., and Furthmüller, J. (1996). Efficient iterative schemes for ab initio total-energy calculations using a plane-wave basis set. Phys. Rev. B *54*, 11169–11186. https://doi.org/10.1103/physrevb.54.11169.

52. Grimme, S., Antony, J., Ehrlich, S., and Krieg, H. (2010). A consistent and accurate ab initio parametrization of density functional dispersion correction (DFT-D) for the 94 elements H-Pu. J. Chem. Phys. *132*, 154104. https://doi.org/10.1063/1.3382344.

53. Monkhorst, H.J., and Pack, J.D. (1976). Special points for Brillouin-zone integrations. Phys. Rev. B *13*, 5188–5192. https://doi.org/10.1103/physrevb.13.5188.

54. Dudarev, S.L., Botton, G.A., Savrasov, S.Y., Humphreys, C.J., and Sutton, A.P. (1998). Electron-energy-loss spectra and the structural stability of nickel oxide: An LSDA+U study. Phys. Rev. B *57*, 1505–1509. https://doi.org/10.1103/physrevb.57.1505.